ARTICLE

Tuning the Oxygen Release Properties of CeO₂-based Catalysts by Metal–Support Interactions for Improved Gasoline Soot Combustion

Ryota Ashikaga,[a] Kazumasa Murata,*[a] Tetsuya Ito,[a] Yuta Yamamoto,[b] Shigeo Arai [b] and Atsushi Satsuma *[a]

To develop highly active soot combustion catalysts for gasoline direct injection exhausts under low oxygen concentration, CeO_2 supported-metal catalysts (M/CeO2, M = Mn, Fe, Co, Ni, Cu, Rh, Pd, and Ag) were examined. Among the catalysts tested, Cu/CeO_2 and Rh/CeO_2 displayed the highest soot combustion activity. By comparing the activities of Cu-based catalysts with and without a $Cu–CeO_2$ interface, the importance of such interface for soot combustion was inferred. The oxygen release rate of CeO_2-based catalysts, enhanced by metal–CeO_2 interactions, was indicated as the controlling factor of catalytic activity. Soot oxidation activity and oxygen release rate were also demonstrated to correlate with metal–oxygen bond energy. Based on the redox properties and structural characteristics of CeO_2-based catalysts, loading CeO_2 with Cu or Rh, which have moderate M–O bond energy, was concluded to be optimal both in terms of the dispersion of supported-metal species and reducibility of the CeO_2-based catalyst.

Introduction

Gasoline direct injection (GDI) is an effective technology for improving both engine power and fuel economy.[1] However, GDI use is associated with an increase in the emissions of particulate matter (PM),[2] which is mainly composed of solid carbon (soot)[2] and causes serious damage to our respiratory system. Therefore, PM emissions are strictly regulated,[2] and the technology for the emission control is developing. A catalytic gasoline particulate filter (GPF) placed in the after-treatment system is an effective system for PM filtration and simultaneous burn-off of accumulated soot by coated catalysts present on the filter's wall. Such ceramic filters are generally applied as diesel particulate filters (DPFs) in diesel engine cars; however, due to the difference in exhaust composition and temperature between diesel and gasoline engines, DPFs cannot be applied as they are directly to gasoline engines. Specifically, diesel engine exhausts contain high amounts of NO_x and oxygen (around 8%), whereas in gasoline engine exhausts the oxygen concentration is

generally 0.5% at most.[3] Therefore, different catalyst designs are needed for GPFs.

Supported Pt catalysts are well known to effectively catalyze soot combustion in diesel exhausts, which contain high concentrations of O_2 and NO_x. In fact, the mentioned Pt-based species catalyze the oxidization of NO to NO_2, which is a highly efficient oxidant in the context of soot combustion.[4] Since the catalytic working conditions of GDI exhausts are quite different from those of diesel exhausts, the catalysts for DPF systems are not effective in the after-treatment of gasoline engine exhausts, which are characterized by low oxygen concentrations.[5] Given the increasing demand for GPFs, over the past few years some studies have been published that focus on soot combustion catalysts for GPFs.

As a result of its excellent oxygen storage capacity (OSC), CeO_2 is an effective catalyst for various oxidation reactions.[6] Li et al. investigated the effect of surface oxygen deficiency on soot combustion catalyzed by CeO_2-ZrO_2.[7] As the Zr content increased, the soot combustion activity decreased, while the amount of surface oxygen defects increased. The authors concluded that the formation of oxygen vacancies is disadvantageous for the catalysis of soot combustion in an oxygen-lean atmosphere, because in such conditions active superoxide (O_2^-) is reduced to the less active capping oxygen (O^{2-}) during oxygen spill-over on a vacancy-rich surface. Liu et al. reported that Ag supported on nanocubic CeO_2 is characterized by good availability of active adsorbed oxygen species (O_2^-), so it displays high catalytic activity and stability.[8] On the other hand, Wu et al. pointed out that an increase in the amount of bulk oxygen defects results in an increase in catalytic activity with respect to soot combustion over Ag/CeO_2.[9] The loading of Nd onto Ag/CeO_2 (to form $Ag/Ce_xNd_{1-x}O_2$) increased the

a. Graduate School of Engineering, Nagoya University, Nagoya 464-8603, Japan.
b. Institute of Materials and Systems for Sustainability, Nagoya University, Nagoya 464-8603, Japan.
*Kazumasa Murata: murata.kazumasa@e.mbox.nagoya-u.ac.jp.

*Atsushi Satsuma: satsuma@chembio.nagoya-u.ac.jp.

catalyst's thermal durability by suppressing Ag particle sintering.[10] Martínez-Munuera *et al*. reported that $Ce_{1-x}Pr_xO_2$ are catalytically active in the oxidation of soot, even under an inert atmosphere.[11] Notably, perovskite catalysts, such as $La_{0.6}Sr_{0.4}BO_3$ (B = Fe, Mn, Ti)[12] and $BaFe_{1-x}Cu_xO_3$ (x = 0–0.4),[13] also displayed high soot combustion activity, as a result of an increase in mobility of lattice oxygen. Although several papers have been published in this field, the factors controlling the activity of soot combustion catalysts for GPFs have not been analyzed in sufficient depth.

The strategy of catalyst design can be found in soot combustion catalyst for DPF. As efficient catalysts for catalytic DPFs, CeO_2-based catalysts have been widely investigated, especially in terms of the promotion of catalytic activity resulting from the loading of transition metals, such as Ag,[14,15] Cr,[16] Mn,[17,18] Fe, [19,20] Co,[20] Cu,[21–24] and Ni.[25] In fact, the loading of these metals generally promotes the formation of reactive oxygen species. Zhang *et al*. reported that the Fe–O–Ce bond in Fe-doped CeO_2 contributes to soot combustion catalysis, a process whereby the redox cycle of Fe^{3+}/Fe^{2+} plays an important role.[20] The oxygen shared bonds of Cr–O–Ce in Cr-doped CeO_2[16] and Cu–O–Ce in $Cu_xCe_{1-x}O_2$[22] are also proposed to act as the active sites in soot combustion catalysis.

Doping CeO_2 with rare-earth elements is also known to enhance soot combustion catalytic activity and improve thermal durability.[26,27] Although for CeO_2-ZrO_2 the effect of OSC on soot combustion is usually discussed, the catalyst surface area[28] and the formation of active oxygen species[28] have been indicated as more important factors. Ag/CeO_2 is a well-studied catalyst, and small Ag particles contacting with CeO_2 promoted catalytic soot combustion.[14,15] Yamazaki *et al*. developed a rice ball-shaped CeO_2–Ag catalyst.[15] This catalyst is composed of Ag particles covered with CeO_2 particles, whereby a large interface area between Ag and CeO_2 exists, which promotes oxygen mobility and the formation of active oxygen species. The self-dispersion of Ag increases Ag–CeO_2 interface area and thus enhances soot oxidation catalytic activity.[29] Notably, although most of these studies focused on the effect of specific transition metals on CeO_2-based catalysts, determining the role of metal–support interactions with a wide range of transition metals is important for an effective catalyst design.

In this study, in order to improve the catalytic activity of CeO_2 for soot combustion under conditions of low oxygen concentration, we systematically investigated the effects of transition metal (Mn, Fe, Co, Ni, Cu, Rh, Pd, and Ag) loading onto CeO_2. Moreover, on the basis of the redox properties and structure of CeO_2-based catalysts, the catalytic activity-controlling factors and the role of metal–support interactions on the catalytic activities was elucidated.

Experimental

Catalyst preparation

CeO_2 (JRC-CEO-3) and SiO_2 (JRC-SIO-12) were supplied by the Catalysis Society of Japan. The other chemicals were purchased from Kishida Chemical Co., Ltd. The precursors used in this study are as follows: $Mn(NO_3)_2 \cdot 6H_2O$, $Fe(NO_3)_3 \cdot 9H_2O$, $Co(NO_3)_2 \cdot 6H_2O$, $Ni(NO_3)_2 \cdot 6H_2O$, $Cu(NO_3)_2 \cdot 3H_2O$, $Rh(NO_3)_3$, $Pd(NO_3)_2$, and $AgNO_3$.

CeO_2-supported metal catalysts are denoted as M/CeO_2 (M = Mn, Fe, Co, Ni, Cu, Rh, Pd, and Ag). M/CeO_2 catalysts were prepared through a conventional impregnation method. The supported metal loading was 5 wt%. Specifically, CeO_2 was added to an aqueous solution of the supported metal precursor, and the resulting solution was stirred for 1 h. Excess water was removed by a rotary evaporator, and the residue thus obtained was dried at 80 °C overnight. The resulting powder was calcined in air at 600 °C for 3 h. M/SiO_2 catalysts (metal loading was 5 wt%) were prepared in the manner just described for M/CeO_2. The physical mixture of $CuO+CeO_2$ was prepared by mixing CeO_2 and CuO (purchased from Kishida Chemical Co. Ltd., Cu metal loading was 5 wt%) in a mortar for 10 min. The error in the soot combustion temperature was within 5 °C.

Characterization

N_2 adsorption measurements

The specific surface area (S_{BET}) of CeO2 and M/CeO2 samples were determined from N_2 adsorption isotherms, which were obtained at −196 °C using a BELSORP-mini II (MicrotracBEL Co.). Prior to analysis, 100 mg of the samples were degassed at 400 °C for 1 h. The surface area was calculated implementing the Brunauer–Emmett–Teller (BET) multipoint method.

X-ray diffraction (XRD) measurements

XRD measurements were performed on a Rigaku Miniflex II/AP with Cu Kα radiation (30 kV, 15 mA).

X-ray photoelectron spectroscopy (XPS) measurements

XPS measurements were conducted using an ESCALAB250 X-ray photoelectron spectrometer (Thermo Fisher Scientific). The C 1s line at 284.8 eV was used to calibrate the binding energies.

Raman spectroscopy measurements

Raman spectra were recorded using a JASCO RMP-330 with a Peltier cooled charge coupled device (CCD) detector using a visible laser (λ = 532 nm). Before conducting the measurements, samples were placed in a flow of 20% H_2/Ar (100 mL min^{-1}) for 20 min at 100 °C or 300 °C and then allowed to cool to room temperature.

Scanning transmission electron microscope-energy dispersive X-ray spectroscopy (STEM-EDX mapping)

EDX mapping images were recorded on a JEM-ARM200F spherical aberration (Cs)-corrected STEM (JEOL Ltd.) operated at 200 kV. Scanning transmission electron microscopy (STEM) images were recorded using a high angle annular dark field (HAADF) detector. The samples were prepared by spreading a drop of methanol suspension of M/CeO_2 catalysts.

X-ray absorption fine structure (XAFS) measurements

Cu K-edge and Ce L_{III}-edge XAFS measurements were performed on BL5S1 beamline at the Aichi Synchrotron Radiation Center. The data were analyzed using the Athena software including the Demeter package. Samples were pretreated in a flow of 20% H_2/N_2 (100 mL min⁻¹) for 20 min at 100 or 200 °C and then sealed in polyethylene bags in an N_2-filled glove box.

Temperature-programmed reduction by hydrogen (H_2-TPR)

H_2-TPR experiments were carried out on a BELCAT B (MicrotracBEL Co.). Before conducting H_2-TPR tests, 50 mg of catalyst samples were pretreated at 500 °C for 30 min in a stream of 100% O_2 (40 mL min⁻¹) and then allowed to cool to ambient temperature. The pretreated samples were subsequently heated from 50 °C (−50 °C in the case of Rh/CeO₂, Pd/CeO₂, and Ag/CeO₂) to 900 °C at a rate of 5 °C min⁻¹ in a stream of 5% H_2/Ar (50 mL min⁻¹). Hydrogen consumption was determined with a thermal conductivity detector (TCD).

Oxygen release/storage measurements

Oxygen release/storage measurements were performed with a thermogravimetric analyzer (TGA). The catalysts were treated at 300 °C in a stream of 10% O_2/N_2 (100 mL min⁻¹) for 30 min. The feed gas was then switched to 5% H_2/N_2 (100 mL min⁻¹) and finally to 10% O_2/N_2 (100 mL min⁻¹), until the weight deviation saturated. The oxygen release/storage capacity[30] and turnover frequency (TOF)[20] of the catalysts were calculated through the following equations (1)–(4):

$$OSC \ (mmol \ g^{-1}) = -\frac{w_{oxi-red}}{w_{cat} \times n_O} \quad (1)$$

Where $w_{oxi-red}$: weight loss of the catalyst before and after the flow of reducing gas (mg); w_{cat}: weight of the catalyst (mg); $and \ n_O$: atomic weight of oxygen (g mmol⁻¹).

$$Oxygen \ release \ rate \ (\mu mol \ g^{-1} \ s^{-1}) = -\frac{DTG_{max-red}}{w_{cat} \times n_O} \quad (2)$$

Where $DTG_{max-red}$: maximum slope of the tangent to the weight loss curve during reduction (mg s⁻¹); w_{cat}: weight of the catalyst (mg); and n_O: atomic weight of oxygen (g μmol⁻¹).

$$Oxygen \ storage \ rate \ (\mu mol \ g^{-1} \ s^{-1}) = \frac{DTG_{max-oxi}}{w_{cat} \times n_O} \quad (3)$$

Where $DTG_{max-oxi}$: maximum slope of the tangent to the weight loss curve during oxidation (mg s⁻¹); w_{cat}: weight of the catalyst (mg); and n_O: atomic weight of oxygen (g μmol⁻¹).

$$TOF \ (\times 10^{-3} \ s^{-1}) = \frac{Oxygen \ release \ rate \ (\mu mol \ g^{-1} \ s^{-1})}{OSC \ (mmol \ g^{-1})} \quad (4)$$

Soot combustion test

The catalytic activity for soot combustion was determined using commercially available carbon black (PrintexV) from Degussa as a model for soot. The average particle size and BET surface area of PrintexV is 25 nm and 92 m² g⁻¹. In figure S1 is reported a TEM image of PrintexV. A 10 mg sample of soot and a 100 mg sample of catalyst were mixed together in a mortar for 10 min to obtain a tight-contact mixture. Notably, tight-contact conditions are often used to evaluate the soot combustion activity.[14,31–34] The catalytic test was carried out with TGA (Rigaku Thermo plus EVO2 thermogravimetric-differential thermal analyzer). In order to remove water adsorbed on the sample, a 10 mg sample of tight-contact mixture was heated from room temperature to 100 °C at a rate of 20 °C min⁻¹ in a stream of 0.5% O_2/N_2 (100 mL min⁻¹) and held at 100 °C for 1 h. The pre-treated sample was then heated from 100 °C to 900 °C at a rate of 5 °C min⁻¹ in a stream of 0.5% O_2/N_2 (100 mL min⁻¹). Notably, the above-described experiment was also carried out in a stream of 10% O_2/N_2 (100 mL min⁻¹).

Results and discussion

Structure of M/CeO₂

The S_{BET} values for M/CeO₂ are reported in Table 1. M/CeO₂ showed lower surface area than that of pure CeO₂. The average surface area of M/CeO₂ was 87 m²g⁻¹ and their variations were within 3.2 m²g⁻¹ (3.7%). Figure 1 shows the XRD patterns of M/CeO₂. XRD lines assignable to fluorite-structured CeO₂ were observed at 2θ = 28.8°, 33.3°, 47.8°, 56.3°, 59.2°, 69.7°, 76.8°, and 79.3° for all catalysts.[23] Each line corresponds to (111), (200), (220), (311), (222), (400), (331), and (420), respectively. The fluorite structure was confirmed to be maintained even after the loading of transition metals onto CeO₂. No line shift was observed for M/CeO₂, which suggests that solid solution formation in the CeO₂ bulk is negligible. Except for Ag/CeO₂, the diffraction lines derived from the supported metal species were not observed, which suggests that the supported metal species are highly dispersed on CeO₂. By contrast, XRD lines attributed to metallic Ag were observed at 2θ = 38.2°, 44.4°, and 64.6° in Ag/CeO₂. These lines correspond to (111), (200), and (220), respectively. The average crystallite size of the metallic Ag particles as calculated by Scherrer's equation was 47.5 nm. We assumed that the metallic Ag particles were poorly dispersed on the CeO₂ support.

XPS results indicated that the oxidation states of the transition metals in the prepared M/CeO₂ species were Mn^{3+} and Mn^{4+}, Fe^{2+} and Fe^{3+}, Co^{2+} and Co^{3+}, Ni^{2+}, Cu^{2+} and Cu^{+}, Rh^{3+}, and Pd^{2+}, for Mn/CeO₂, Fe/CeO₂, Co/CeO₂, Ni/CeO₂, Cu/CeO₂, Rh/CeO₂, and Pd/CeO₂, respectively (Figure S2). As for Ag/CeO₂, the oxidation state of Ag could not be determined by XPS because of the overlap of the Ag 3d peaks assignable to Ag^{+} and Ag^{0}. XPS results identified that supported metal species were mainly present on CeO₂ as metal oxides, except in the case of Ag/CeO₂. Notably, after loading the transition metals, no significant change in the oxidation state of cerium and in the

ARTICLE   **Journal Name**

binding energy of CeO_2 lattice oxygen was observed in any of the M/CeO_2 catalysts (Figure S3).

Table 1. Specific surface areas (S_{BET}), oxygen storage capacity (OSC), and oxygen release/storage performances of CeO_2 and M/CeO_2.

Catalyst	S_{BET} / m^2 g^{-1}	OSC / mmol g^{-1}	Oxygen release rate / µmol g^{-1} s^{-1}	Oxygen storage rate / µmol g^{-1} s^{-1}
CeO_2	108	0.0074	0.13	0.18
Mn/CeO_2	83	0.38	1.5	8.8
Fe/CeO_2	71	0.23	0.72	8.4
Co/CeO_2	81	0.95	2.3	11.9
Ni/CeO_2	88	0.53	1.5	9.9
Cu/CeO_2	92	0.73	7.3	10.5
Rh/CeO_2	99	0.84	7.5	14.7
Pd/CeO_2	97	0.51	5.3	11.3
Ag/CeO_2	85	0.073	1.0	12.5

Figure S4 shows a TEM image of the Cu/CeO_2 catalyst. CeO_2 particles approximately 10 nm in size are shown to aggregate to form second-order particles, whereas Cu species are not clearly observed. STEM-EDX images confirmed the dispersion of supported metal species (Figures 2 and S5). As can be evinced from Figures 2d and e, respectively, large Pd and Ag particles were observed in Pd/CeO_2 and Ag/CeO_2. The particle diameters were around 5–10 nm. Smaller Rh particles (<5 nm) were observed in Rh/CeO_2. The existence of highly dispersed clusters was confirmed for Cu/CeO_2 and Fe/CeO_2.
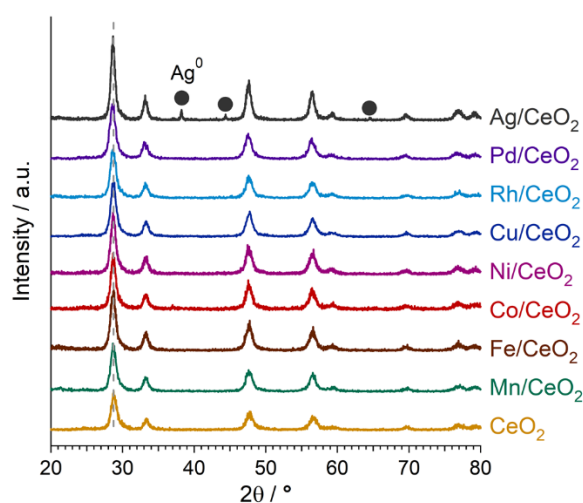
Figure 1. X-ray diffraction patterns of as-prepared M/CeO_2.
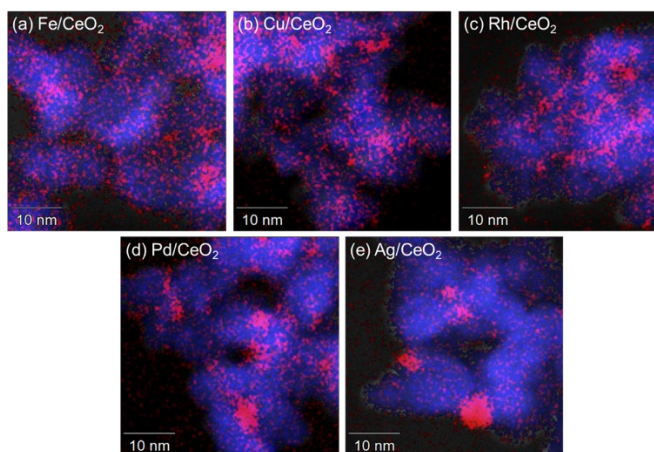
Figure 2. High-magnification scanning transmission electron microscope-energy dispersive X-ray spectroscopy mapping images of as-prepared (a) Fe/CeO_2, (b) Cu/CeO_2, (c) Rh/CeO_2, (d) Pd/CeO_2, and (e) Ag/CeO_2. Red: Fe, Cu, Rh, Pd, and Ag, Blue: Ce.

This dispersion of supported-metal species was in agreement with Raman spectroscopy data (Figure S6). Although the Raman bands of PdO[35] and Rh_2O_3[36] were observed in Pd/CeO_2 and Rh/CeO_2, Cu and Fe oxides could not be detected by Raman spectroscopy (Figure S6). The results indicate that Cu and Fe oxides were present on CeO_2 as small clusters. Only the F_{2g} band of CeO_2 was observed in Ag/CeO_2. Since Ag_2O is characterized by a broad Raman band at 490 cm^{-1} and AgO by a strong Raman band at 429 cm^{-1},[37] the experimental spectrum suggests that Ag in Ag/CeO_2 is present as Raman-inactive Ag metal. This conclusion is in good agreement with the XRD pattern, which included the diffraction lines of metallic silver.

Soot combustion activity of M/CeO_2

Figure 3a shows the soot conversion on M/CeO_2 as a function of the temperature under conditions simulating those in GDI exhaust in a flow of 0.5% O_2/N_2. When the soot was heated in the presence of CeO_2, the temperature of soot combustion shifted to lower values by about 300 °C. Moreover, in the presence of CeO_2-supported metal catalysts, soot combustion temperature decreased further by between 10 and 100 °C with respect to pure CeO_2. The effect of supported-metal catalysts on the light-off temperature of soot combustion was evaluated using the parameter T_{10}, the temperature at which 10% of soot has undergone conversion. The values of T_{10} for Cu/CeO_2 and Rh/CeO_2 were about 70 °C lower than that for pure CeO_2. As can be evinced from the data in Figure 3b, the soot combustion activities of M/CeO_2 catalysts increase in the following order: None (pure CeO_2) < Fe < Mn < Ag < Ni < Pd < Co < Cu and Rh. Notably, this order was different from that observed under simulated diesel exhaust conditions, whereby oxygen concentration was 10%, (Figure S7). In that case, the T_{10} value order was as follows: None < Mn < Fe < Ni, Co, and Pd < Ag < Cu < Rh. Nevertheless, regardless of the oxygen concentration, Cu/CeO_2 and Rh/CeO_2 displayed the highest soot combustion

activity. Table S1 summarized the soot combustion temperatures under simulated GPF and DPF conditions measured in this work and reported in the literature. Although the reaction conditions are slightly different from each other, use of Cu/CeO_2 and Rh/CeO_2 was associated with the lowest combustion temperatures across reports.
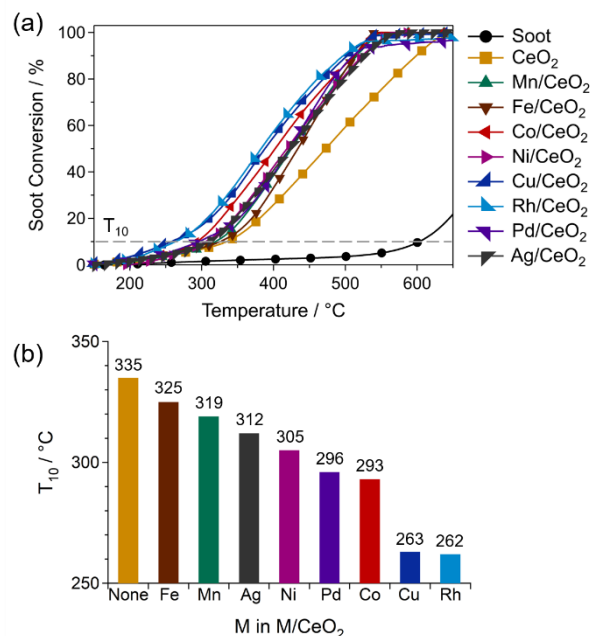
Figure 3. (a) Soot conversion *versus* temperature. (b) Temperature at which 10% of soot has been converted (T_{10}), in the presence of M/CeO_2 catalysts under a flow of 0.5% O_2/N_2.

The observed remarkable decrease in soot combustion temperature associated with using M/CeO_2 was not linked solely to the presence of the supported transition metals. In fact, when the chemically inert SiO_2 was used as the support, the obtained catalysts did not display remarkable soot combustion activity. As can be evinced from Figure S8, the T_{10} of pure soot combustion was 603 °C, whereas the T_{10} values for most M/SiO_2 catalysts were 500 °C or higher. Indeed, even though Ag/SiO_2 was the most effective catalyst for soot combustion, its T_{10} value (394 °C) was higher than that of pure CeO_2 (335 °C). The results can be interpreted as indicating that the high soot combustion catalytic activity of M/CeO_2 catalysts descends from the presence of the metal–CeO_2 interface and/or the influence that the CeO_2 support exerts on the transition metals.

Effect of Cu–Ce interactions on soot combustion catalytic activity

In order to investigate the catalytic importance of Cu–Ce interactions, a $CuO+CeO_2$ system lacking the Cu–CeO_2 interface was prepared by physical mixing. Figure 4 shows the soot combustion catalytic activity of a series of Cu-based catalysts having different Cu–Ce interfaces (or no such interface). The T_{10} values for Cu/SiO_2 and $CuO+CeO_2$ were higher than that for CeO_2. This result clearly indicates that the high soot combustion catalytic activity of Cu/CeO_2 is not caused by the presence of

the supported CuO_x species itself, but by the close contact between Cu and CeO_2.
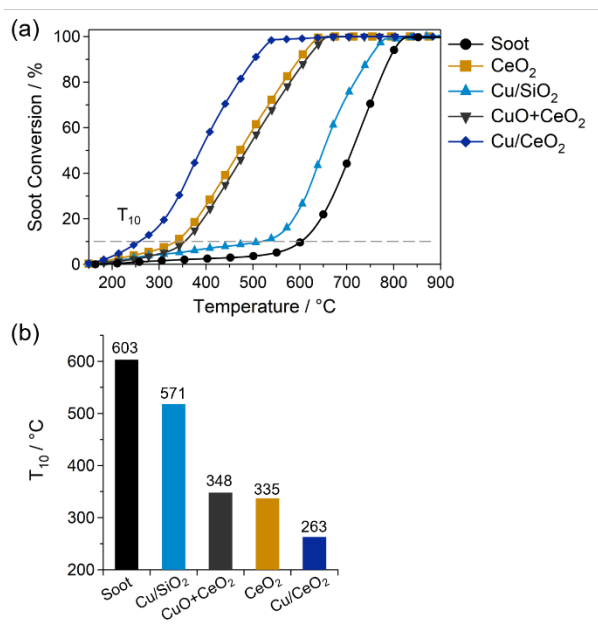
Figure 4. (a) Soot conversion versus temperature. (b) Temperature at which 10% of soot has been converted (T_{10}) in the presence of different Cu-based catalysts under a flow of 0.5% O_2/N_2.

H_2-TPR profiles of CeO_2 and various Cu-based catalysts are shown in Figure 5. The profile of CeO_2 was characterized by two broad peaks at 300–500 °C and 600–850 °C, which were attributed to the reduction of CeO_2 surface and bulk, respectively.[27] In the case of $CuO+CeO_2$, three reduction peaks were observed at 170 °C, 300–500 °C, and 600–850 °C. The peak at 170 °C, which was similar to its counterpart observed for Cu/SiO_2, was attributed to the reduction of CuO_x.[38] In the case of Cu/CeO_2, two sharp reduction peaks were observed at 84 °C and 148 °C, whereas the peak associated with the reduction of the CeO_2 surface at 300–500 °C was absent. Evidence thus suggests that the surface of CeO_2 was activated by the Cu species, so that the relevant reduction peak may have shifted below 200 °C. The H_2 consumption of each catalyst was estimated from the area of the reduction peak at 50–250 °C (Table S1). The theoretical H_2 consumption associated with the reduction of $Cu^{+2}O$ to Cu^0 metal is 0.79 mmol g^{-1}. In fact, H_2 consumption by Cu/CeO_2 (1.54 mmol g^{-1}) was substantially larger than the theoretical value for CuO reduction, indicating that the reduction of not only CuO, but also of CeO_2, occurred below 200 °C in the case of Cu/CeO_2.[39,40] In order to confirm the assignment of the low-temperature reduction peak observed for Cu/CeO_2, XAFS and Raman spectroscopy measurements were conducted. The Cu K-edge X-ray absorption near edge structure (XANES) spectra reported in Figure S9 clearly demonstrate the presence of Cu^{2+} species in as-prepared Cu/CeO_2. The Cu K-edge XANES spectra of Cu/CeO_2 after H_2 reduction at 100 °C displayed no difference to that of as-prepared Cu/CeO_2. Conversely, the XANES spectrum of

Cu/CeO_2 recorded after H_2 reduction at 200 °C indicated that most Cu species had undergone reduction from Cu^{2+} to Cu^0 between 100 and 200 °C. Based on linear combination fitting (LCF) analysis of the Ce L_{III}-edge XANES spectra, the fraction of Ce^{3+} in Cu/CeO_2 was estimated to be 1.2 and 3.2%, after H_2 reduction at 100 and 200 °C, respectively (Figure S10). Figure 5 shows the Raman spectra of CeO_2, $Cu+CeO_2$, and Cu/CeO_2 after H_2 reduction at 100 °C. The spectra of all samples exhibited the F_{2g} mode associated with a fluorite cubic CeO_2 structure. Notably, an additional band at 593 cm^{-1} was observed for Cu/CeO_2. This band has been attributed to oxygen vacancies (O_v) in the CeO_2 lattice.[41] Therefore, in the case of Cu/CeO_2, it was confirmed that lattice oxygen release from CeO_2 had occurred during H_2 reduction at 100 °C. The evidence just discussed indicates, therefore, that the reduction peaks at 84 and 148 °C in the H_2-TPR profile of Cu/CeO_2 are mainly due to the reduction of CeO_2 and CuO_x clusters, respectively. Indeed, CeO_2 became more easily reducible as a result of the $Cu-CeO_2$ interaction.
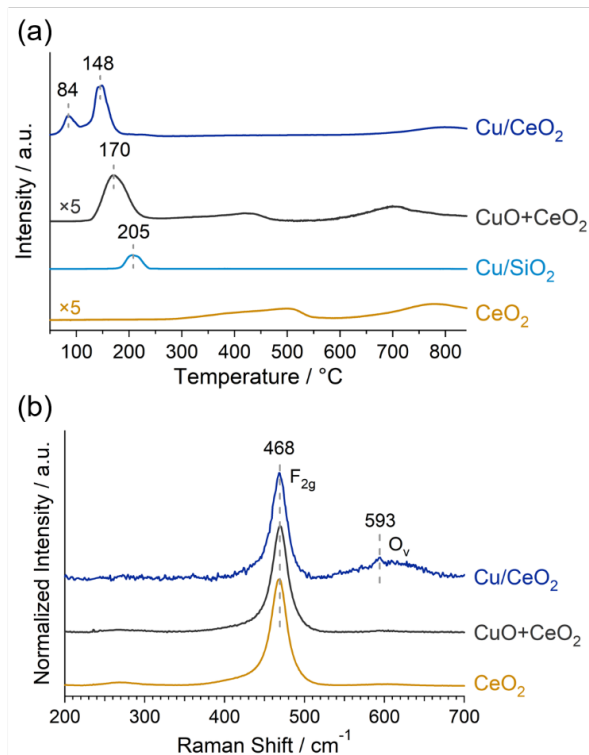
Figure 5. (a) H_2-TPR profiles of CeO_2 and Cu-based catalysts. (b) Raman spectra of CeO_2 and Cu-based catalysts after undergoing H_2 reduction at 100 °C.

Relationship between oxygen release capacity and catalytic activity in M/CeO_2

Similarly to the oxidation reactions occurring over other metal oxide catalysts,[42] the soot combustion reaction over CeO_2 has been proposed to proceed through a Mars-van Krevelen mechanism.[19] In addition, soot combustion has been reported to proceed at the soot–CeO_2 interface.[43] Therefore, in CeO_2-based catalysts, the specific surface area of the catalysts and the

transfer of CeO_2 lattice oxygen to soot have been reported to be the activity-controlling factors in catalytic soot combustion.[27,28,44] The catalytic activity-controlling factors of M/CeO_2 were thus investigated. Figure S11 shows the relationship between catalytic soot combustion activity and M/CeO_2 surface area. The catalytic activity was not well correlated to surface area. It is indicated that the soot combustion activity cannot be rationalized by the S_{BET} value of the catalysts.

The rate and capacity of oxygen release/storage of M/CeO_2 were determined measuring by TGA the weight change associated with switching between a reducing atmosphere (flowing gas: 5% H_2/N_2) and an oxidizing one (flowing gas: 10% O_2/N_2) at 300 °C.[30] Figure S12 shows the weight change of Cu/CeO_2 as a typical result. The weight loss due to oxygen release from CeO_2 was observed under a reducing atmosphere; the weight increase due to oxygen storage into CeO_2 was instead observed under an oxidizing atmosphere. The oxygen release/storage capacity of M/CeO_2 was calculated with equations (1)–(3) reported above. The rates and capacities of oxygen release/storage of M/CeO_2 are listed in Table 1. Since the rate of oxygen release is slower than that of storage for all the M/CeO_2 catalysts, the dependence of the catalytic activity on OSC and on the oxygen release rate were examined.

As can be evinced from the data reported in Figure 6, in GDI conditions (0.5% O_2/N_2) the value of T_{10}, which was used as an index of catalytic soot combustion activity, correlated well with the value of the oxygen release rate. By contrast, T_{10} values did not display a strong correlation with OSC (Figure S13) values; in fact, although Co/CeO_2 was characterized by a higher OSC than Cu/CeO_2 and Rh/CeO_2, it displayed lower catalytic soot combustion activity (higher T_{10}) than the other two catalysts. Evidence thus indicated that the oxygen release rate is the controlling factor in catalytic soot combustion activity; in other words, increases in oxygen release rate result in increases in soot combustion activity. Indeed, a dependence of the combustion activity on the oxygen release rate is reasonable, given that, in low oxygen concentration conditions, lattice oxygen is expected to play a more important role in soot combustion than oxygen adsorbed from the gas phase. On the other hand, the correlation between the value of T_{10} and that of the oxygen release rate was weaker under GPF conditions (10% O_2/N_2) than under GDI conditions (0.5% O_2/N_2) (Figure S14). This difference can be attributed to the more significant contribution of gas-phase or weakly adsorbed oxygen to soot combustion in the high-oxygen-concentration case.
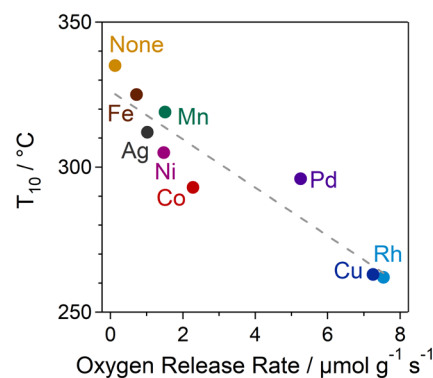
Figure 6. Relationship between catalytic soot combustion activity under 0.5% O_2/N_2 and oxygen release rate of M/CeO_2. The coefficient of determination $R^2 = 0.87$.

Structure–Activity Relationship in M/CeO_2

According to the discussion above on the effect of Cu–Ce interactions on catalytic soot combustion activity, the supported metals are expected to play a role in tuning the reducibility of CeO_2 via the metal–CeO_2 interaction.[45] The strength of the interaction or chemical bond between metal and support has been reported to be efficiently predicted by a descriptor like the oxide formation enthalpy of the supported metal.[46–49] Thus, the oxygen release rate as a controlling factor of soot combustion was plotted against the energy of the metal–oxygen bond of the supported metal (Figure 7). Notably, the M–O bond energy values were estimated from the metal oxide formation enthalpy per oxygen atom.[50]
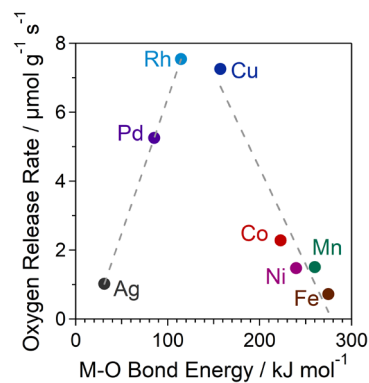
Figure 7. Relationship between the oxygen release rate of M/CeO_2 and the metal–oxygen bond energy.

The oxygen release rate showed a volcanic correlation with the M–O bond energy, with Cu and Rh at the top. Figure 7 demonstrates that moderate M–O bond energies of the supported-metals are required to observe high oxygen release rates for M/CeO_2. The right-hand slope implies that the oxygen release rate decreases as the M–O bond energy increases. In other words, the increase in reducibility of CeO_2 by the supported metals with lower M–O bond energies could be explained by the formation of weaker M–O–Ce bonds. The promoting effect of supported metals on the reducibility of

CeO_2 was estimated from H_2-TPR data (Figure S15). In all M/CeO_2 catalysts, the pure CeO_2 peak near 500 °C, which is associated with surface CeO_2 reduction, shifted to lower temperatures, indicating an increase in reducibility due to the metal–CeO_2 interactions. In addition, the experimental value of H_2 consumption for almost all M/CeO_2 catalysts was larger than the theoretical H_2 consumption of the supported metal species (Table S2). Except for pure CeO_2, the Raman spectra recorded after H_2 reduction at 300 °C comprised the O_v band, which is associated with vacancies in the CeO_2 lattice (Figure S16). Evidence thus clearly suggests that the reduction peak below 550 °C is due not just to the reduction of the supported metal but also to the reduction of the CeO_2 surface. Notably, the temperature of the first reduction of the CeO_2-supported metal catalysts decreased in the following order: Fe > Co > Mn > Ni > Cu (> Ag) > Rh > Pd, which matches almost perfectly the strength order of M–O bonds (Figure S17). Taking the diffraction lines of metallic Ag in XRD into account, the reduction of Ag^+ to metallic Ag also occurred below −50 °C.

The mentioned H_2-TPR results support the idea that lattice oxygen can be easily released from the metal–CeO_2 interface when the M–O binding energies are low. However, in the left-hand slope of Figure 7, the oxygen release rate of M/CeO_2 decreased as the M–O binding energy decreased. When the oxygen release rate per OSC (TOF calculated using equation (4) above) was plotted against the M–O bond energy, the TOF monotonically increased as the M–O bond energy decreased (Figure 8).
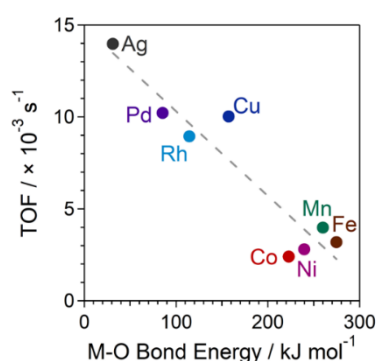
Figure 8. Relationship between the TOF of M/CeO_2 and the metal–oxygen bond energy.

According to previous reports, the OSC and oxidation activity of CeO_2-supported metal catalysts depend on the number of metal–CeO_2 interfaces.[51,52] Furthermore, Ag, which is characterized by a low M–O bond energy, has been reported to easily form aggregates due to the weakness of its interaction with the support. On the other hand, supported metals like Fe, Co, Ni, and Cu, which are characterized by high M–O bond energies, are reported to be highly dispersed on the oxide support.[48] Therefore, the left slope in Figure 7 suggests a decrease in the metal–CeO_2 interface sites. Based on STEM-EDX mapping, the dispersion of the supported metal species on CeO_2 decreases in the following order: Fe ≈ Cu > Rh > Pd > Ag. Therefore, the left slope can reasonably be explained by a decrease of the metal–CeO_2 interface. CeO_2-supported Cu and Rh catalysts, which are characterized by moderate M–O bond energies, displayed high soot combustion activities, due to the formation of metal–CeO_2 interfaces from which lattice oxygen can be easily released. On the other hand, CeO_2-supported Fe, Mn, Ni, and Co, which are characterized by high M–O bond energies, have relatively strong M–O–Ce bonds, so that the promotion of oxygen release of CeO_2 is weak. Finally, CeO_2-supported Pd and Ag, characterized by low M–O bond energies, displayed lower activity because it is unfavorable in their case to generate the metal–CeO_2 interface, given their weak interaction with CeO_2.

Conclusions

M/CeO_2 (M = Mn, Fe, Co, Ni, Cu, Rh, Pd, and Ag) catalysts were prepared and used to catalyze the combustion of soot under GDI exhaust conditions (i.e., low oxygen concentration). The catalytic soot combustion activity of CeO_2 was enhanced by metal–CeO_2 interactions. Cu/CeO_2 and Rh/CeO_2 proved to be the most suitable soot combustion catalyst candidates for use in a gasoline particulate filter. The importance of the Cu–CeO_2 interface was demonstrated, and oxygen was observed to be released from the Cu–CeO_2 interfaces or CuO_x cluster at lower temperatures than from pure CeO_2. Cu and Rh were also suggested to display the highest oxygen release rate due to their moderate M–O bond energies. In fact, the loading of metals with higher M–O bond energies (Fe, Mn, Ni, and Co) led to the formation of relatively strong M–O–Ce bonds, resulting in a weak activation of the CeO_2 surface. Since the loading of the metals with lower M–O bond energies (Pd and Ag) rendered unfavorable the formation of a metal–CeO_2 interface, due to the weakness of the interaction with CeO_2, their soot combustion activities were lower than those observed for Cu/CeO_2 and Rh/CeO_2. Tuning the oxygen release properties of CeO_2 via metal–support interactions is an effective approach to increasing the soot combustion activity of CeO_2-based catalysts under low oxygen concentration conditions, and the selection of supported metal species with moderate M–O bond energies is important.

Conflicts of interest

There are no conflicts to declare.

Acknowledgements

References

1. F. Zhao, M. C. Lai and D. L. Harrington, *Prog. Energy Combust. Sci.*, 1999, **25**, 437–562.

2. B. Liang, Y. Ge, J. Tan, X. Han, L. Gao, L. Hao, W. Ye and P. Dai, *J. Aerosol Sci.*, 2013, **57**, 22–31.

3. D. Fennell, J. Herreros and A. Tsolakis, *Int. J. Hydrogen Energy*, 2014, **39**, 5153–5162.

4. A. Bueno-López, *Appl. Catal. B Environ.*, 2014, **146**, 1–11.

5. H. Wang, S. Liu, Z. Zhao, X. Zou, M. Liu, W. Liu, X. Wu and D. Weng, *Catal. Sci. Technol.*, 2017, **7**, 2129–2139.

6. T. Montini, M. Melchionna, M. Monai and P. Fornasiero, *Chem. Rev.*, 2016, **116**, 5987–6041.

7. P. Li, X. Chen, Y. Li and J. W. Schwank, *Catal. Today*, 2019, **327**, 90–115.

8. S. Liu, X. Wu, W. Liu, W. Chen, R. Ran, M. Li and D. Weng, *J. Catal.*, 2016, **337**, 188–198.

9. S. Wu, Y. Yang, C. Lu, Y. Ma, S. Yuan and G. Qian, *Eur. J. Inorg. Chem.*, 2018, **2018**, 2944–2951.

10. Y. Gao, A. Duan, S. Liu, X. Wu, W. Liu, M. Li, S. Chen, X. Wang and D. Weng, *Appl. Catal. B Environ.*, 2017, **203**, 116–126.

11. J. C. Martínez-Munuera, M. Zoccoli, J. Giménez-Mañogil and A. García-García, *Appl. Catal. B Environ.*, 2019, **245**, 706–720.

12. W. Y. Hernández, M. N. Tsampas, C. Zhao, A. Boreave, F. Bosselet and P. Vernoux, *Catal. Today*, 2015, **258**, 525–534.

13. C. Moreno-Marcos, V. Torregrosa-Rivero, V. Albaladejo-Fuentes, M. S. Sánchez-Adsuar and M. J. Illán-Gómez, *Top. Catal.*, 2019, **62**, 413–418.

14. K. ichi Shimizu, H. Kawachi and A. Satsuma, *Appl. Catal. B Environ.*, 2010, **96**, 169–175.

15. K. Yamazaki, T. Kayama, F. Dong and H. Shinjoh, *J. Catal.*, 2011, **282**, 289–298.

16. X. Li, S. Wei, Z. Zhang, Y. Zhang, Z. Wang, Q. Su and X. Gao, *Catal. Today*, 2011, **175**, 112–116.

17. Q. Liang, X. Wu, D. Weng and H. Xu, *Catal. Today*, 2008, **139**, 113–118.

18. H. Zhao, X. Zhou, M. Wang, Z. Xie, H. Chen and J. Shi, *RSC Adv.*, 2017, **7**, 3233–3239.

19. E. Aneggi, C. de Leitenburg, G. Dolcetti and A. Trovarelli, *Catal. Today*, 2006, **114**, 40–47.

20. Z. Zhang, D. Han, S. Wei and Y. Zhang, *J. Catal.*, 2010, **276**, 16–23.

21. X. Wu, Q. Liang, D. Weng and Z. Lu, *Catal. Commun.*, 2007, **8**, 2110–2114.

22. B. Cui, S. Yan, Y. Xia, K. Li, S. Li, D. Wang, Y. Ye and Y. Q. Liu, *Appl. Catal. A Gen.*, 2019, **578**, 20–29.

23. P. Sudarsanam, B. Hillary, B. Mallesham, B. G. Rao, M. H. Amin, A. Nafady, A. M. Alsalme, B. M. Reddy and S. K. Bhargava, *Langmuir*, 2016, **32**, 2208–2215.

24. S. Liu, X. Wu, D. Weng and R. Ran, *J. Rare Earths*, 2015, **33**, 567–590.

25. E. P. Mahofa, T. B. Narsaiah and P. Kumar, *Int. J. Eng. Res. Technol.*, 2014, **3**, 48–51.

26. K. Krishna, A. Bueno-López, M. Makkee and J. A. Moulijn, *Appl. Catal. B Environ.*, 2007, **75**, 210–220.

27. K. Krishna, A. Bueno-López, M. Makkee and J. A. Moulijn, *Appl. Catal. B Environ.*, 2007, **75**, 189–200.

28. E. Aneggi, C. De Leitenburg and A. Trovarelli, *Catal. Today*, 2012, **181**, 108–115.

29. K. Shimizu, H. Kawachi, S. I. Komai, K. Yoshida, Y. Sasaki and A. Satsuma, *Catal. Today*, 2011, **175**, 93–99.

30. S. H. Song, J. Moon, J. H. Kim, J. Hong, J. H. Lee, H. W. Lee, B. K. Kim and H. Kim, *Acta Mater.*, 2016, **113**, 206–212.

31. S. Putla, M. H. Amin, B. M. Reddy, A. Nafady, K. A. Al Farhan and S. K. Bhargava, *ACS Appl. Mater. Interfaces*, 2015, **7**, 16525–16535.

32. D. Mukherjee, B. G. Rao and B. M. Reddy, *Appl. Catal. B, Environ.*, 2016, **197**, 105–115.

33. M. Machida, Y. Murata, K. Kishikawa, D. Zhang and K. Ikeue, *Chem. Mater.*, 2008, **20**, 4489–4494.

34. K. Mori, K. Watanabe, T. Sato and H. Yamashita, *ChemPhysChem*, 2015, **16**, 1347–1351.

35. A. Baylet, P. Marécot, D. Duprez, P. Castellazzi, G. Groppi and P. Forzatti, *Phys. Chem. Chem. Phys.*, 2011, **13**, 4607–4613.

36. S. Parres-Esclapez, I. Such-Basañez, M. J. Illán-Gómez, C. Salinas-Martínez De Lecea and A. Bueno-López, *J. Catal.*, 2010, **276**, 390–401.

37. G. I. N. Waterhouse, G. A. Bowmaker and J. B. Metson, *Phys. Chem. Chem. Phys.*, 2001, **3**, 3838–3845.

38. K. N. Rao, P. Venkataswamy and B. M. Reddy, *Ind. Eng. Chem. Res.*, 2011, **50**, 11960–11969.

39. H. Muroyama, S. Hano, T. Matsui and K. Eguchi, *Catal. Today*, 2010, **153**, 133–135.

40. H. Shang, X. Zhang, J. Xu and Y. Han, *Front. Chem. Sci. Eng.*, 2017, **11**, 603–612.

41. E. Sartoretti, C. Novara, F. Giorgis, M. Piumetti, S. Bensaid, N. Russo and D. Fino, *Sci. Rep.*, 2019, **9**, 9–13.

42. *Modern Heterogeneous Catalysis*, 2017.

43. S. B. Simonsen, S. Dahl, E. Johnson and S. Helveg, *J. Catal.*, 2008, **255**, 1–5.

44. A. Bueno-López, K. Krishna, B. van der Linden, G. Mul, J. A. Moulijn and M. Makkee, *Catal. Today*, 2007, **121**, 237–245.

45. H. J. Kim, G. Jang, D. Shin and J. Woo, *ChemCatChem*, 2020, 11–26.

46. C. T. Campbell and J. R. V. Sellers, *Faraday Discuss.*, 2013, **162**, 9–30.

47. M. E. Strayer, T. P. Senftle, J. P. Winterstein, N. M. Vargas-Barbosa, R. Sharma, R. M. Rioux, M. J. Janik and T. E. Mallouk, *J. Am. Chem. Soc.*, 2015, **137**, 16216–16224.

48. N. J. O'Connor, A. S. M. Jonayat, M. J. Janik and T. P. Senftle, *Nat. Catal.*, 2018, **1**, 531–539.

49. K. Murata, D. Kosuge, J. Ohyama, Y. Mahara, Y. Yamamoto, S. Arai and A. Satsuma, *ACS Catal.*, 2020, **10**, 1381–1387.

50. D. R. Lide, Ed., *CRC Handbook of Chemistry and Physics*, CRC Press, Boca Raton, 89th edn., 2009.

51. M. Cargnello, V. V. T. Doan-Nguyen, T. R. Gordon, R. E. Diaz, E. A. Stach, R. J. Gorte, P. Fornasiero and C. B. Murray, *Science*, 2013, **341**, 771–773.

52. A. M. Gänzler, M. Casapu, F. Maurer, H. Störmer, D. Gerthsen, G. Ferré, P. Vernoux, B. Bornmann, R. Frahm, V. Murzin, M. Nachtegaal, M. Votsmeier and J. D. Grunwaldt, *ACS Catal.*, 2018, **8**, 4800–4811.